Engineering Geology 345 (2025) 107875

Contents lists available at ScienceDirect

Engineering Geology

journal homepage: www.elsevier.com/locate/enggeo

Numerical investigation on the response of ground-reinforced embankments under repeated impact

Xin Li [a,b], Zhiwei Gao [a,*], Liang Lu [c]

[a] Glasgow Computational Engineering Centre (GCEC), James Watt School of Engineering, University of Glasgow, Glasgow G12 8QQ, UK
[b] School of Civil and Hydraulic Engineering, Qinghai University, Xining 810016, China
[c] School of Civil Engineering, Chongqing University, Chongqing 400045, China

ARTICLE INFO

Keywords:
Rockfall impact
Sand density
Constitutive model
Ground-reinforced embankments
Finite element modelling

ABSTRACT

Ground-reinforced embankment (GRE) is an effective and environmentally friendly technique of rockfall intervention. These earth structures are built with layers of compacted soil alternated with geotextiles, geogrills, metallic wire stripes or nets. GREs are designed to sustain repeated rock impact during their service life, but there is very little experimental or numerical research on the GRE response under such impact conditions. A comprehensive numerical investigation of GRE response under repeated rock impact is carried out. The GRE is built with several layers of sand wrapped by geosynthetics. An advanced elastoplastic constitutive model for sand is adopted. For the GREs built with dense and loose sand, most of the impact energy is dissipated by plastic deformation in the soil. Sand density has a dominant influence on the deformation and failure mechanism of GREs. During repeated impacts, elements near the impact location fail with increasing mean effective stress and Mises stress in dense sand. However, soil elements reach failure as the mean effective stress decreases and the Mises stress increases. There is much less deformation accumulation in GRE when the void ratio is lower as the soil has higher stiffness and shear strength. After multiple impacts, shear bands form in loose sand but strain localisation mainly occurs at the impact point for dense sand.

1. Introduction

Rockfall is characterised by rock material's sudden release and movement down a slope or cliff face. This hazard stems from various geological, climatic, and human-induced factors, making it a complex phenomenon to understand and mitigate. Geological factors such as the presence of steep slopes, weak rock formations, and fractures or faults contribute to the instability of rock masses, increasing the likelihood of rockfalls (Peila et al., 2007; Guzzetti et al., 2005; Moos et al., 2022; Bertrand et al., 2013). Weathering processes, including freeze-thaw cycles and rainfall, weaken the cohesion between rocks, facilitating their detachment and subsequent fall (Pérez-Rey et al., 2019). Human activities such as mining, quarrying, and construction can also destabilise rock formations, altering natural slopes and triggering rockfalls (Hungr et al., 2014). Stoffel et al. (2024) have found that continuous global warming is driving more rockfall incidents in the Swiss Alps. Rockfalls pose a direct risk to human life, particularly in areas with high population density or frequented by tourists. Moreover, rockfalls can damage infrastructure such as roads, railways, buildings, and utility networks, disrupting transportation systems and essential services (Agliardi et al., 2009). The economic consequences of such damage can be substantial, requiring costly repair and maintenance efforts.

Once the mechanism of rockfall (detachment point, rockfall trajectory and deposition of rock debris) and potential impact on infrastructure/human habitats are defined, measures for rockfall protection need to be designed, which include either active or passive ones. The active measures are designed to prevent the detachment of rock from rock slopes, such as rock bolts, rock dowels and rock netting (Bertolo et al., 2009; Peila and Ronco, 2009; Tran et al., 2013; Wyllie, 2015). The passive ones are constructed to intercept and stop the blocks, thus eliminating or reducing the impact of rockfall hazards. Examples of passive measures include rock shelters, catch fences and GREs. Rockfall shelters consist of reinforced concrete structures with roofs covered by a layer of absorbing material, typically soil backfill (Lambert and Bourrier, 2013; Moon et al., 2014; Bourrier et al., 2015; Turner and Schuster, 2012). Rockfall catch fences are constructed with steel wires, posts, ropes and anchors. This steel mesh acts as a barrier to intercept moving blocks and transfers stopping forces to ground anchors. In designing

* Corresponding author.
E-mail address: zhiwei.gao@glasgow.ac.uk (Z. Gao).

https://doi.org/10.1016/j.enggeo.2024.107875
Received 1 August 2024; Received in revised form 28 November 2024; Accepted 15 December 2024
Available online 18 December 2024

Table 1
Model parameters for Fontainebleau sand.

Group	Parameter	Value
Elasticity	ν	0.25
	G_0	100
	n	0.55
Critical state	e_Γ	0.825
	λ_c	0.055
	ξ	0.46
	$\phi_u/^\circ$	33.2
Shear-sliding	k_p	0.0015
	A_d	0.55
	m_1	2.5
	m_2	2.8
Compression	λ'	0.25
	p_{c0}/kPa	15,000
Grain breakage parameters	e_{refu}	0.296
	e_{ref0}	0.825
	b/kPa	12,000
	ρ	4

high-energy fences, some energy-dissipation devices can be installed to reduce the forces being transferred to ground anchors (Tran et al., 2013). GREs are used when the rock blocks have volumes or speeds that are great enough to break through the maximum resistance of traditional catch fences (Lambert and Bourrier, 2013; Peila et al., 2007). According to Volkwein and Gerber (2011), the choice of rockfall protection measures depends on their energy absorption capacities. For example, rigid fences are suitable for low-energy impacts up to approximately 100 kJ, while barrier systems can handle impacts ranging from 10 kJ to 10,000 kJ. Retaining walls or GREs, designed for higher energy levels, can withstand impacts ranging from 10 kJ to 100,000 kJ. GREs have two main advantages over the other passive measures: (a) They have a much higher energy absorption capacity and can sustain multiple rockfall impacts (Peila et al., 2007; Lambert and Kister, 2018); (b) They are easier and cheaper to build and repair than other passive measures because local soils can be used in construction and the reinforced materials used are light-weight (Brunet et al., 2009; Xiao et al., 2023; Celik, 2023).

There have been extensive experimental and numerical studies on the response of GREs under rockfall impact, including full-scale tests (e.g., Aminata et al., 2008; Peila et al., 2007; Peila, 2012), small-scale tests (e.g., Kister and Fontana, 2011; Lambert and Kister, 2017; Korini et al., 2021) and numerical modelling (Di Prisco and Vecchiotti, 2006; Shen et al., 2019; Yan et al., 2020; Oggeri et al., 2021; Lu et al., 2021). It is found that numerical modelling is a powerful tool for analysing the response of GRE and assisting the design. The modelling of GREs in this study has been designed based on existing research in which static element test results are used for dynamic modelling (Lu et al., 2021; Gao et al., 2023; Xiao et al., 2023). However, the existing numerical studies have two major limitations. First, the mechanical behaviour of soil in GREs has not been properly accounted for. The Mohr-Coulomb model has been frequently used (Lu et al., 2021; Ma et al., 2024), which is not capable of capturing the highly nonlinear stress-strain relationship of soils (Gao et al., 2014; Liang et al., 2020; Wang et al., 2024; Yao et al., 2004). Secondly, most studies have focused on the response of GREs under a single rockfall impact, while GREs are designed for multiple impacts (Peila et al., 2007; Xiao et al., 2023; Maheshwari et al., 2024; Maheshwari and Bhowmik, 2024). This study aims to use an advanced elastoplastic sand model to simulate the deformation and failure mechanism of GREs under repeated impacts and to provide important theoretical support for the design of GREs in the field.

Numerical modelling of repeated rockfall impacts on GREs is presented in this study. A GRE built with several layers of sand wrapped in geosynthetics is modelled. A double-yield-surface (DYS) sand model accounting for the effect of soil state (density and stress) is used (Jin et al., 2018). The paper is organised as follows. The DYS model and its predictive capability are introduced first to facilitate the result interpretation. Following this, the numerical modelling of repeated rock impact on GREs is presented. The GRE response is analysed in terms of block velocity and energy evolution, impact stress distribution, impact force evolution and deformation localisation. Implications of the findings for GRE design are discussed.

2. The Constitutive Model

The yield function for shear sliding f_1 is expressed as (Jin et al., 2018),

$$f_1 = \frac{q}{p} - \frac{M_p \varepsilon_d^p}{k_p + \varepsilon_d^p} = 0 \tag{1}$$

where q is the deviatoric stress ($q = \sqrt{\frac{3}{2} s_{ij} s_{ji}}$, with $s_{ij} = \sigma_{ij} - p\delta_{ij}$), σ_{ij} is the stress tensor, $p = \sigma_{ii}/3$ is the mean effective stress, δ_{ij} is the Kronecker delta (= 1 for $i = j$, and = 0 for $i \neq j$), ε_d^p is the deviatoric plastic strain, k_p is a model parameter related to the plastic shear modulus; $M_p = 6sin\phi_p/\left(3 - sin\phi_p\right)$ is the virtual peak stress ratio that varies with the peak friction angle ϕ_p expressed in terms of the critical friction angle ϕ_u and the current void ratio e,

$$tan\phi_p = tan\phi_u \left(\frac{e_c}{e}\right)^{m_1} \tag{2}$$

where m_1 is material constant and the critical state void ratio e_c is expressed as,

$$e_c = e_\Gamma \, exp\left[-\lambda_c \left(\frac{p}{p_a}\right)^{\xi}\right] \tag{3}$$

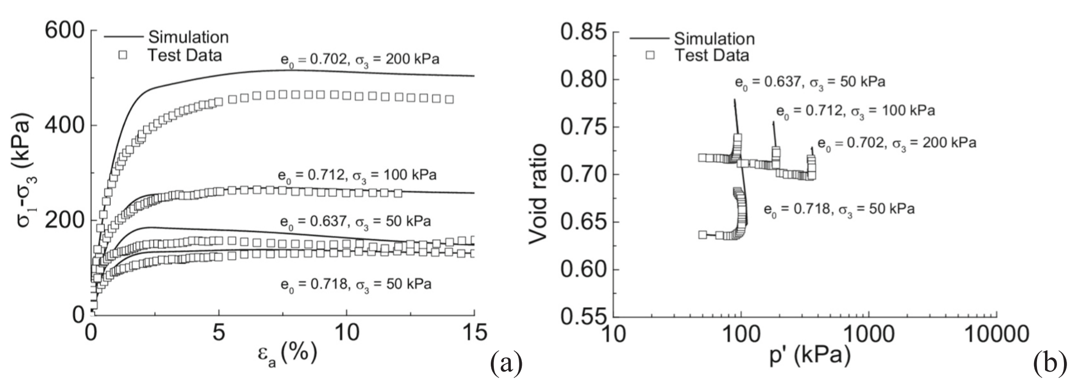

Fig. 1. Comparison between the model simulations and test results of Fontainebleau NE34 sand in drained triaxial compression tests: (a) deviatoric stress versus axial strain, and (b) void ratio versus mean effective stress.

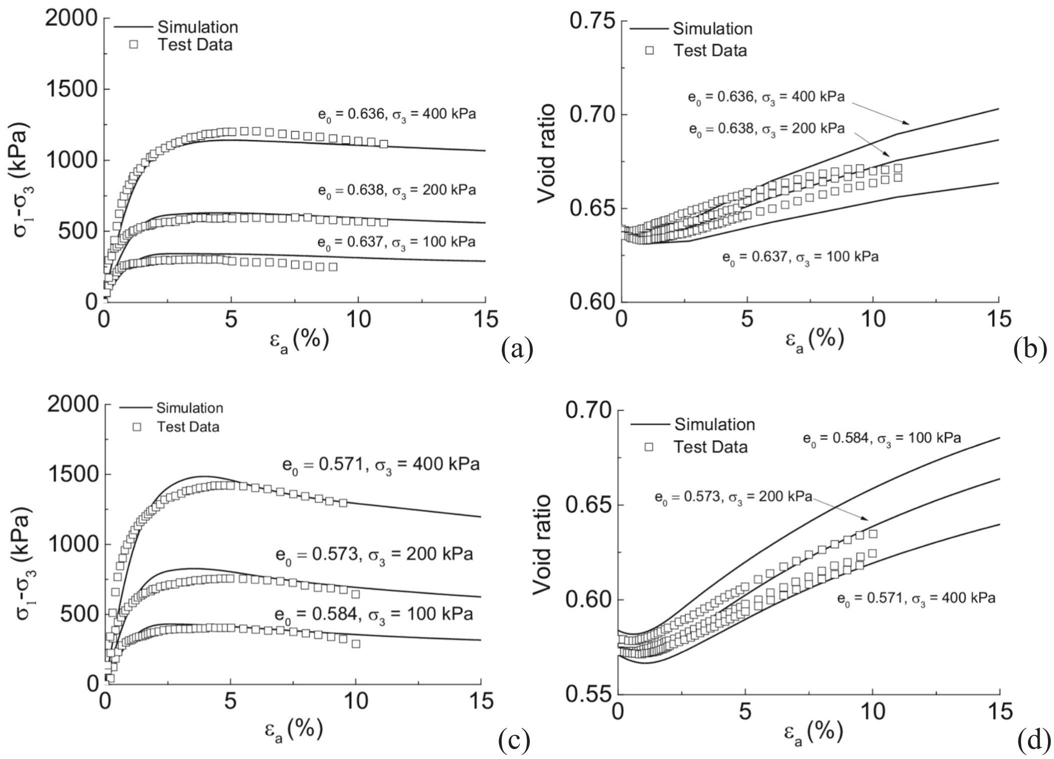

Fig. 2. Model prediction of Fontainebleau NE34 sand in drained triaxial compression tests: (a) and (c) deviatoric stress versus axial strain; and (b) and (d) void ratio versus axial strain.

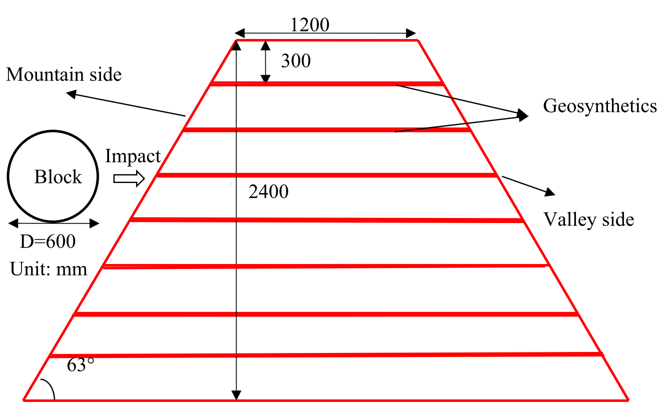

Fig. 3. The cross-section of the model embankment.

where p_a is atmospheric pressure (101 kPa), λ_c and ξ are material parameters and e_r is a variable that evolves with particle breakage which will be given below. The partial differential equations for the plastic potential surface g_1 is given by,

$$\frac{\partial g_1}{\partial \sigma_{ij}} = \frac{\partial g_1}{\partial p}\frac{\partial p}{\partial \sigma_{ij}} + \frac{\partial g_1}{\partial q}\frac{\partial q}{\partial \sigma_{ij}} = A_d\left(M_{pt} - \frac{q}{p}\right)\frac{\partial p}{\partial \sigma_{ij}} + \frac{\partial q}{\partial \sigma_{ij}} \tag{4}$$

where A_d is a model parameter, $M_{pt} = 6sin\phi_{pt}/\left(3 - sin\phi_{pt}\right)$ with ϕ_{pt} being expressed as,

$$tan\phi_{pt} = tan\phi_u\left(\frac{e_c}{e}\right)^{-m_2} \tag{5}$$

where m_2 is a model parameter. Note that the explicit formulation for g_1 cannot be derived based on Eqs. (4) and (5). The second yield function f_2 and the plastic potential surface g_2 of the model which is used to describe the normal compression behaviour of sand are expressed as,

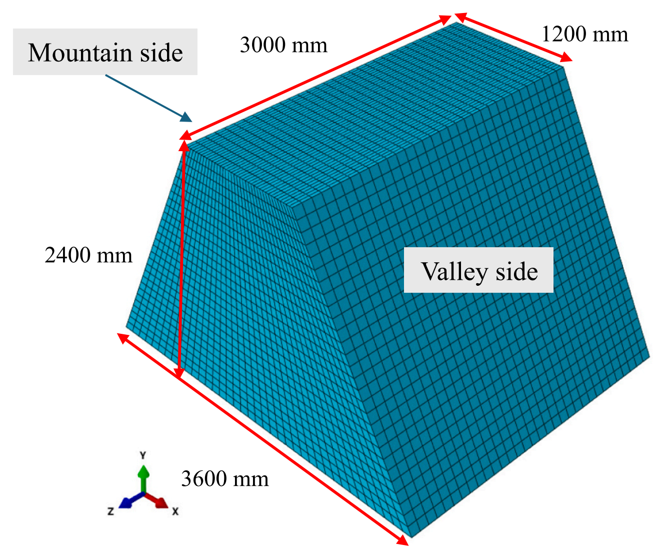

Fig. 4. Mesh size of GRE used in the simulations.

Table 2
Properties for the block, geosynthetic and sand.

	Density (kg/m^3)	Young's modulus (MPa)	Poisson's ratio ν
Block	7830	/	/
Geosynthetic	1400	180	0.25
Sand	1630	/	/

$$f_2 = g_2 = \frac{1}{2}\left(\frac{q}{M_p p}\right)^3 p + p - p_c \tag{6}$$

Table 3
Summary of impact tests.

Simulation numbers		Impact velocity (m/s)	Impact energy (kJ)	Accumulated energy (kJ)
e_0 = 0.6	e_0 = 0.8			
1–1	2–1	10	44.25	44.25
1–2	2–2	10	44.25	88.50
1–3	2–3	10	44.25	132.75

where p_c is the hardening parameter controlling the size of the yield surface. The yield surface expands with the increment of plastic volumetric strain increment $d\varepsilon_v^p$,

$$dp_c = p_c \frac{1+e}{(\lambda' - G')e} d\varepsilon_v^p \tag{7}$$

where the parameter λ' controls the slope of the compression line, $G' = p(1+e)/G$ is a normalised value calculated by elastic bulk modulus G which is defined as,

$$G = G_0 p_a \frac{(2.97-e)^2}{(1+e)} \left(\frac{p}{p_a}\right)^n \tag{8}$$

where G_0 and n are elastic model parameters. The particle breakage is modelled by considering the evolution of e_Γ in Eq. (3) with the grain breakage index B_r^*

$$e_\Gamma = e_{refu} + (e_{ref0} - e_{refu}) exp(-\rho B_r^*) \tag{9}$$

where e_{ref0} and e_{refu} are the virgin and ultimate reference critical void ratios for the virgin soil without grain breakage, ρ is the material parameter and B_r^* is expressed as,

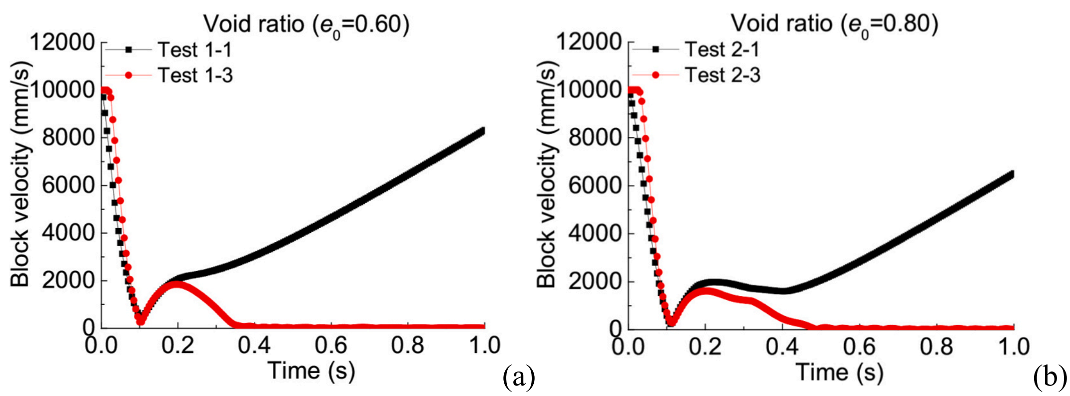

Fig. 5. Evolution of block velocity during the first and third impacts: (a) initial void ratio of sand $e_0 = 0.6$; (b) initial void ratio of sand $e_0 = 0.8$.

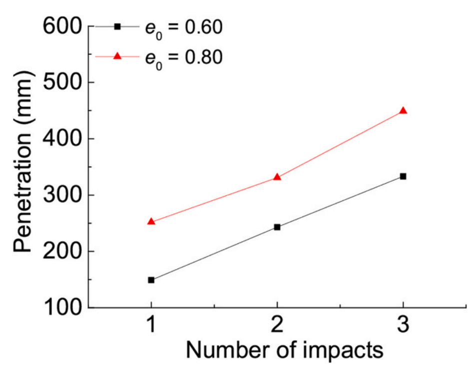

Fig. 6. Penetration depth of the block in GREs different void ratios.

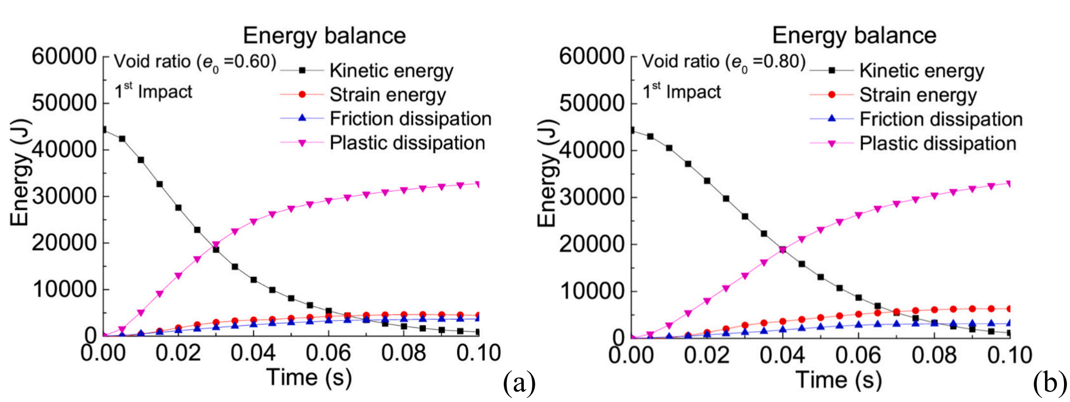

Fig. 7. Energy evolution in the first impact: (a) initial void ratio of sand $e_0 = 0.6$; (b) initial void ratio of sand $e_0 = 0.8$.

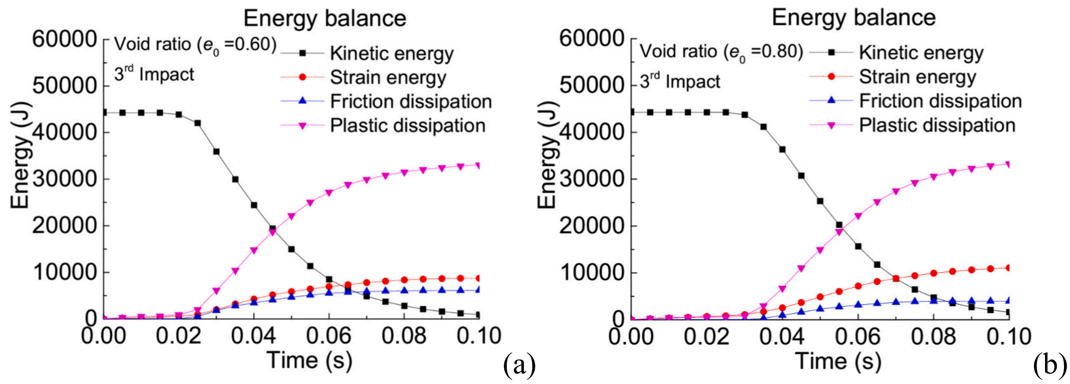

Fig. 8. Energy evolution in the third impact: (a) initial void ratio of sand $e_0 = 0.6$; (b) initial void ratio of sand $e_0 = 0.8$.

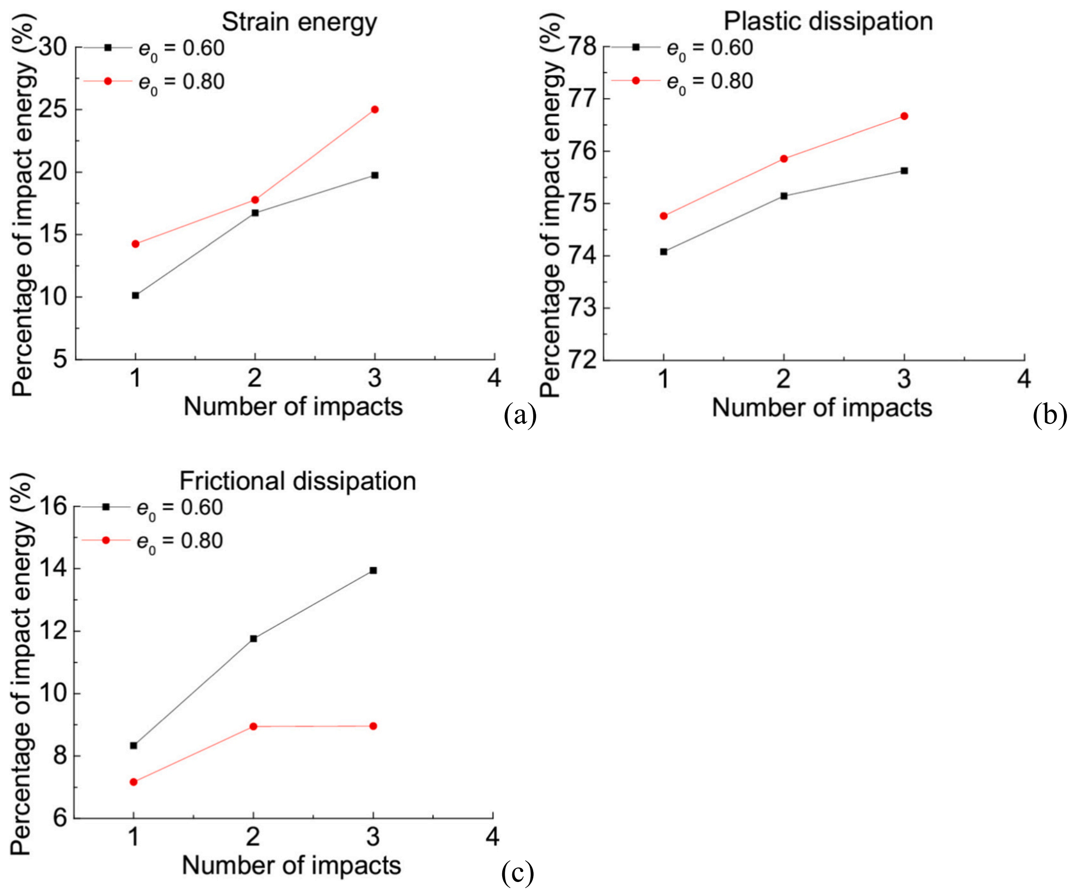

Fig. 9. Effect of repeated impacts on the energy evolution in GREs with different void ratios: (a) strain energy; (b) plastic dissipation; (c) Frictional dissipation.

$$B_r^* = \frac{w_p}{b + w_p} \tag{10}$$

where $w_p = \int \left(p\langle d\varepsilon_v^p\rangle + qd\varepsilon_d^p\right)$ is the plastic work, are the McCauley brackets and b is a material constant controlling the evolution rate of the grain breakage index.

The increment of total strain $d\varepsilon_{ij}$ is composed of the elastic and plastic strain parts,

$$d\varepsilon_{ij} = d\varepsilon_{ij}^e + d\varepsilon_{ij}^p \tag{11}$$

The elastic and plastic strain increment tensor can be expressed as,

$$d\varepsilon_{ij}^e = \frac{1+\nu}{E}d\sigma_{ij} - \frac{\nu}{E}d\sigma_{kk}\delta_{ij} \tag{12}$$

$$d\varepsilon_{ij}^p = \left(d\varepsilon_{ij}^p\right)_1 + \left(d\varepsilon_{ij}^p\right)_2 = d\lambda_1\frac{\partial g_1}{d\sigma_{ij}} + d\lambda_2\frac{\partial g_2}{d\sigma_{ij}} \tag{13}$$

where ν and $E = 3G(1 - 2\nu)$ are Poisson's ratio and Young's modulus, $d\lambda_1$ and $d\lambda_2$ are the plastic multipliers representing the shear sliding and compression components, respectively. Derivation of the constitutive equations can be found in Jin et al. (2018).

This model has been implemented in the finite element package ABAQUS/Explicit through the user-material (VUMAT) (Dassault Systèmes, 2023). The cutting plane algorithm of the DYS model is employed in the model implementation (Jin et al., 2018) which is a semi-implicit scheme that can guarantee accurate and efficient results even for large time steps. The model parameters for Fontainebleau sand are given in Table 1. The model predictions of Fontainebleau sand

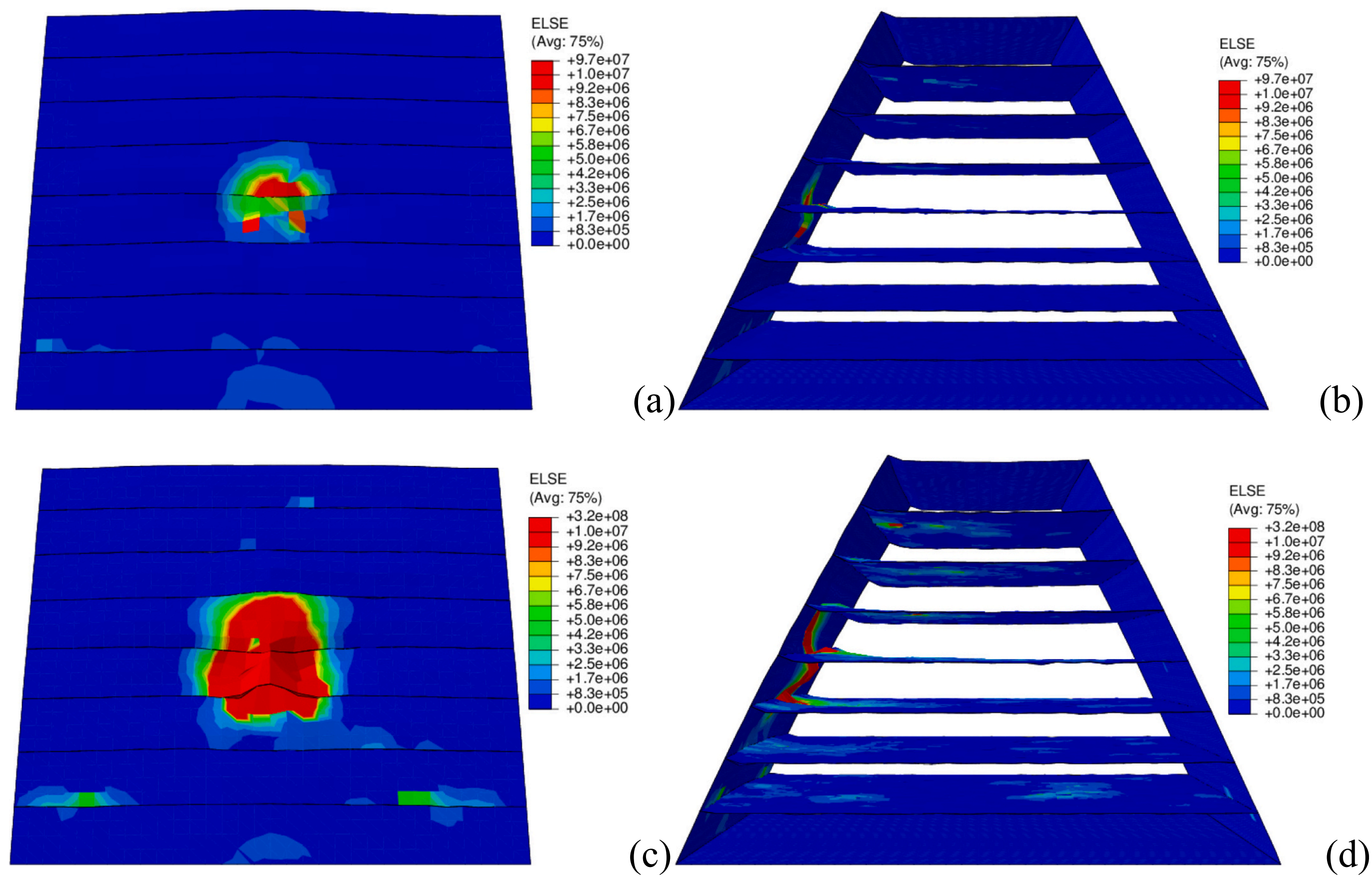

Fig. 10. Strain energy distribution in geosynthetics with $e_0 = 0.6$ after the first impact (a, b) the third impact (c, d).

behaviour in drained triaxial compression tests are shown in Figs. 1 and 2 (Jin et al., 2018). The test data is from Andria-Ntoanina et al. (2010). More validation results can be found in Jin et al. (2018).

3. Finite element modelling of rockfall impact on GRE

The GRE modelled here is built using 8 layers of sand wrapped by geosynthetics. The dimension and mesh size of the GRE used in simulations are shown in Fig. 3 and Fig. 4, respectively. The slope angle is chosen based on the suggested values reported in the literature (Peila et al., 2007; Ronco et al., 2009). The properties of the block, geosynthetics and sand are given in Table 2.

The block density specified for the block in Table 2 is based on the assumption that the block is made of steel. The pressure-dependent elastic parameters for sand are given in Table 1. Sand is modelled using the eight-node brick element with reduced integration (C3D8R). The geosynthetics with a thickness of 0.25 mm are modelled using 4-node quadrilateral membrane elements with reduced integration (M3D4R). The thickness and the mechanical parameters of the geosynthetics used here are the same as those in the Lu et al. (2021). The friction coefficient for contacting geosynthetic surfaces is 0.46 (Ronco et al., 2009; Oggeri et al., 2021). The steel block with a diameter of 600 mm is simulated using rigid 3D bilinear quadrilateral elements (R3D4). Steel is used following the tests by Lu et al. (2021). The friction coefficient between the block and geosynthetics is 0.45 (Uesugi et al., 1989). The bottom of GRE is fully fixed while all the other sides are free to deform. Following the definitions in existing studies (Ronco et al., 2009; Lambert and Bourrier, 2013; Oggeri et al., 2021), the impact side of the GRE is called the mountain side and the opposite one is called the valley side (Fig. 4).

Since the embankment has three free surfaces with two inclined, the conventional K_0 procedure cannot be used to generate the initial stress state. Therefore, the gravitational loading method is adopted (Gao et al., 2021). Specifically, the embankment is first assumed to be an elastic material with a large elastic modulus and Poisson's ratio ν_e. The ν_e can be calculated from a lateral earth pressure coefficient $K_0 = \nu_e/(1-\nu_e) = 0.48$ (Jin et al., 2018). The gravitational body force is then applied to the embankment to generate the initial stress state. During the impact modelling, the elastoplastic model with parameters listed in Table 1 is used. The impact tests simulated are summarised in Table 3. In the subsequent impacts, the block is first removed and the GRE is allowed to deform under gravity until the system reaches equilibrium. The equilibrium stress state is then imported to the system as the initial stress state before impact. The initial void ratio of sand is $e_0 = 0.6$ ($D_r = 83\%$) and $e_0 = 0.8$ ($D_r = 21\%$) in the simulations (Table 3). It should be mentioned that loose soil is not recommended in the practical design of GREs, loose sand is chosen here to illustrate the effect of density on the GRE response.

GREs built with coarse sand have higher energy absorption capacity as the sand strength and stiffness are higher (Lu et al., 2021). Since there is no triaxial test data on coarse sand for getting the model parameters, Fontainebleau sand with fine particles is used in this study. Consequently, the impact energy used in this study is relatively low (Table 3). However, the findings are expected to be valid for GREs built with coarse sand.

3.1. Block velocity and energy evolution under repeated impacts

Fig. 5 shows the evolution of block velocity in the first and third impact for GREs with different initial void ratios. The block bounces back after the first impact, and the velocity increase after impact (at about 0.1 s) is driven by the free fall of the block. In the following two

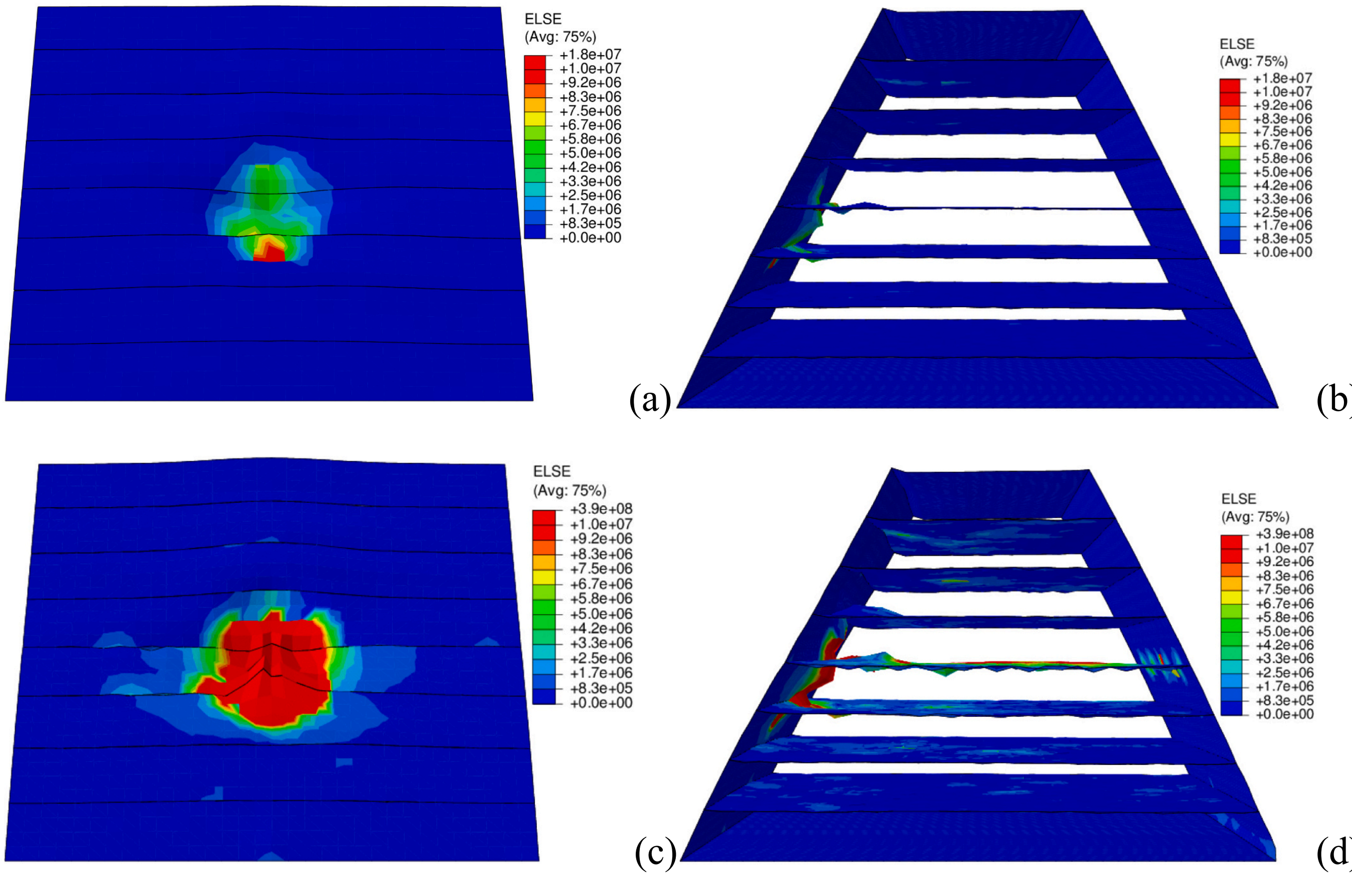

Fig. 11. Strain energy distribution in geosynthetics with $e_0 = 0.8$ after the first impact (a, b) the third impact (c, d).

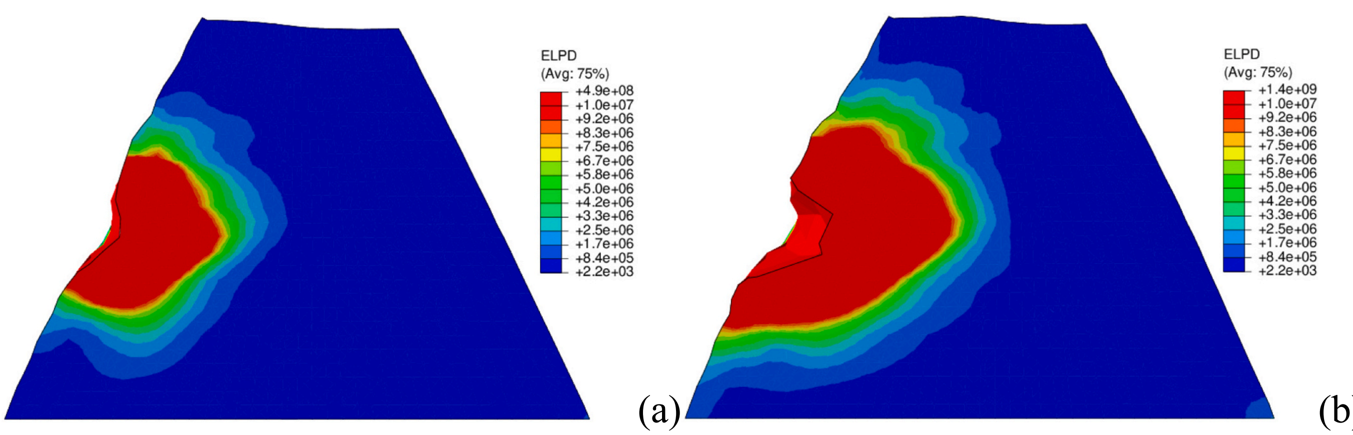

Fig. 12. Plastic dissipation distribution in GREs with $e_0 = 0.6$ after the first impact (a and b) and the third impact (c and d).

impacts, the block gets embedded in the GRE and the velocity reaches 0 at the end. The penetration depth of the block is higher in loose sand. It increases with the number of impacts (Fig. 6).

During the impacts, part of or all the impact energy (initial kinetic energy of the block) is converted into plastic dissipation in the sand, friction dissipation (friction between geosynthetics and between geosynthetics and block) and strain energy in both sand and geosynthetics (Figs. 7 and 8). It is found that over 74 % of the impact energy is dissipated due to plastic deformation in sand. Frictional dissipation and strain energy account for about 6–10 % and 10–15 % of the impact energy, respectively. This is in agreement with the previous studies (Ronco et al., 2009; Lambert and Bourrier, 2013; Oggeri et al., 2021). In the second and third impacts, the block becomes embedded within the GRE, resulting in higher percentages of plastic dissipation, frictional dissipation, and strain energy for both loose and dense sand (Fig. 9). More plastic dissipation and strain energy occurs in loose sand due to more deformation in the soil. Meanwhile, frictional dissipation in loose sand is very small (Fig. 9). This indicates that GREs built with less dense sand are more effective in dissipating the impact energy. However, as will be shown later, there is much more deformation in GREs with loose sand.

Fig. 10 and Fig. 11 show the effect of sand void ratio on strain energy in geosynthetics. After the first impact, strain energy in the geosynthetics with dense sand appears in the fourth and fifth layers of geosynthetics on the mountain-side, with a small amount of strain energy also appearing in the seventh and eighth layers near the bottom of

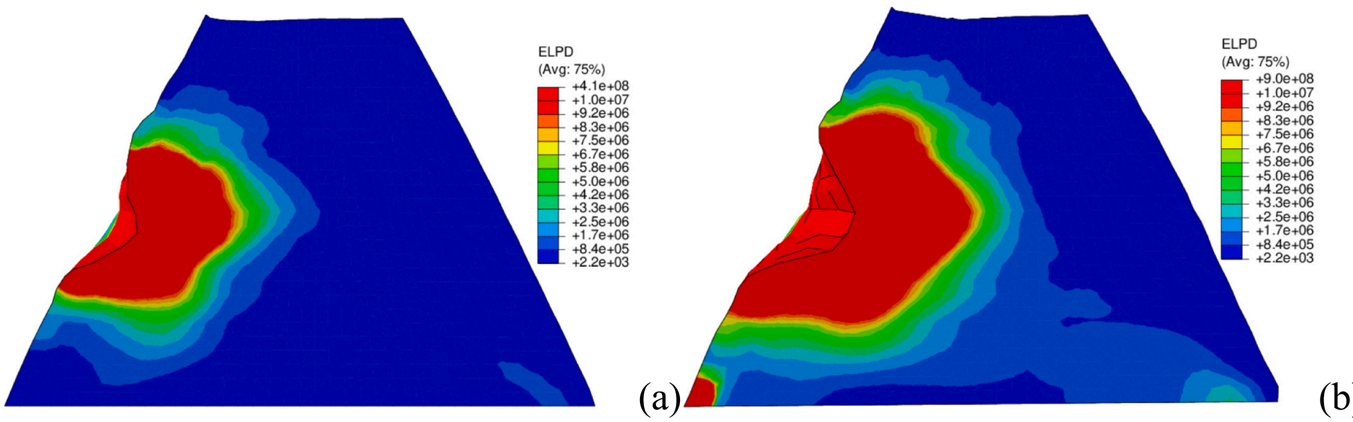

Fig. 13. Plastic dissipation distribution in GREs with $e_0 = 0.8$ after the first impact (a and b) and the third impact (c and d).

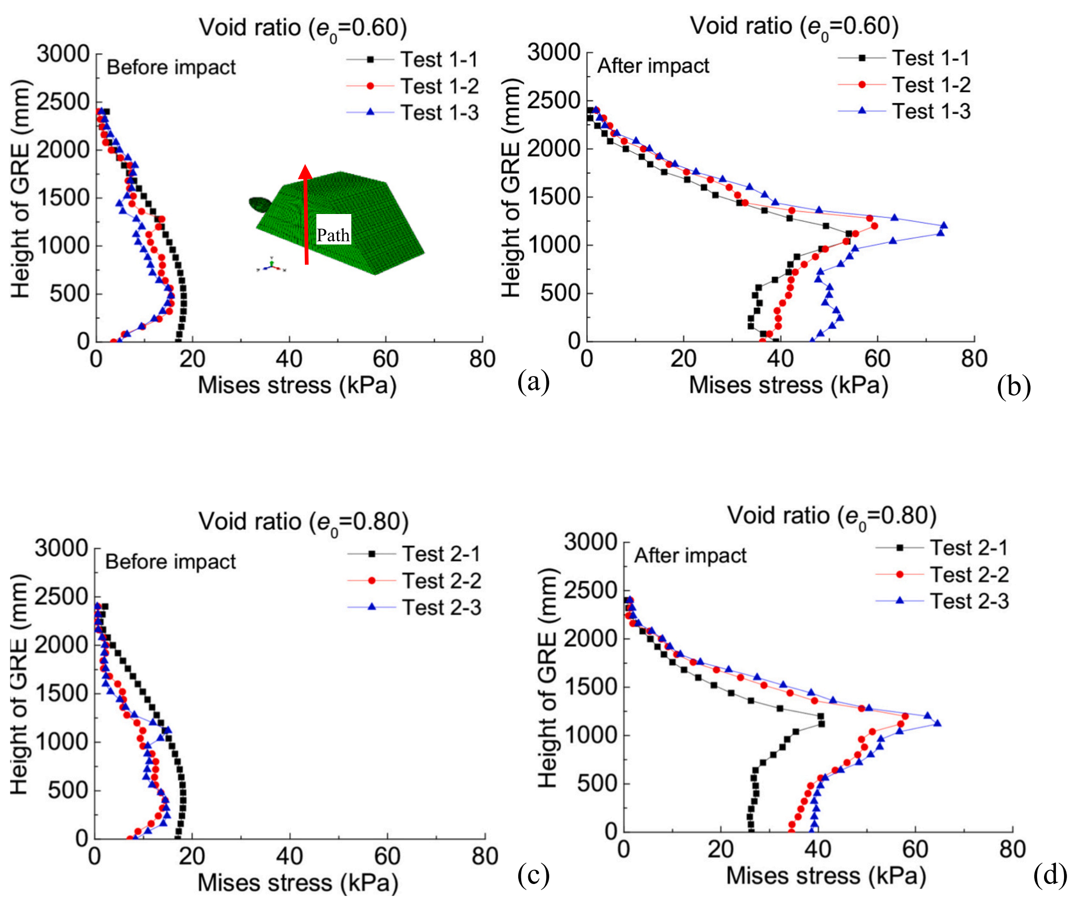

Fig. 14. Effect of repeated impacts on the Mises stress in GREs: (a and b) $e_0 = 0.6$; (c and d) $e_0 = 0.8$.

the GRE (Fig. 10a). For the GRE built with loose sand, strain energy appears only in the fourth, fifth, and sixth layers of geosynthetic (Fig. 11a). In the side view of geosynthetics changes shown in Fig. 11 (d), significant deformation appears in the fourth and fifth layers of geosynthetics for the loose sand when compared to the dense sand in Fig. 10 (d), and strain energy also appears on the valley-side of the GRE. This is due to that the GRE built with loose sand undergoes greater deformation after being impacted by a block. Additionally, after the first impact, the magnitude of strain energy is greater in the GRE with dense sand (Fig. 10a and Fig. 11a). But after the third impact, the magnitude of strain energy is greater in the GRE with loose sand (Fig. 10c and Fig. 11c). Therefore, under repeated impact conditions, the efficiency of geosynthetics in the GRE with loose sand is significantly improved, allowing it to absorb more impact energy.

Figs. 12 and 13 show that the magnitude of plastic dissipation is greater for the GRE with dense sand regardless of whether it is the first or the third impact compared to the GRE with loose sand. For GRE with dense sand, the region of plastic dissipation is mainly concentrated in the vicinity of the block impact area (Fig. 12). However, as the sand void ratio increases, the region of plastic dissipation not only concentrates near the block impact area but also extends towards the toe of the slopes on the mountain-side and valley-side of the GRE (Fig. 13). After the third impact (Fig. 13d), significant plastic dissipation appears at the toe of the slope on the mountain-side. Therefore, repeated impacts have a greater

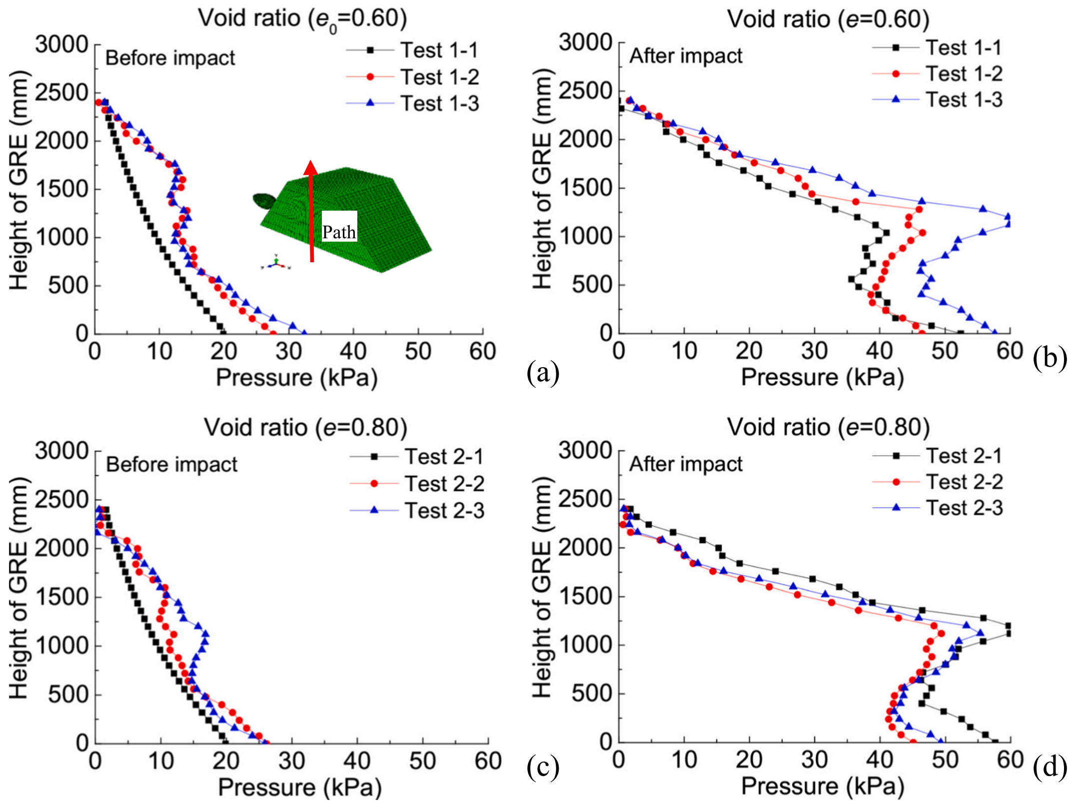

Fig. 15. Effect of repeated impacts on pressure in GREs: (a and b) $e_0 = 0.6$; (c and d) $e_0 = 0.8$.

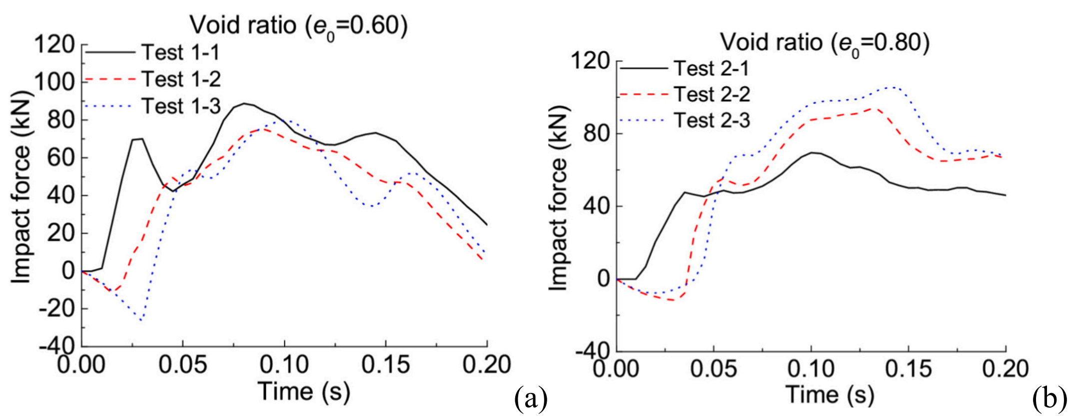

Fig. 16. Effect of repeated impacts on impact force in GREs: (a) $e_0 = 0.6$; (b) $e_0 = 0.8$.

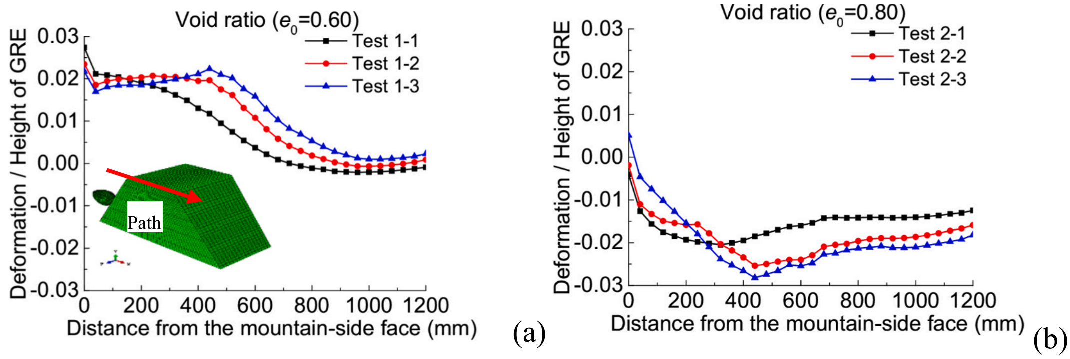

Fig. 17. Effect of repeated impacts on the crest deformation of GREs with varied void ratio: (a) $e_0 = 0.6$ and (b) $e_0 = 0.8$.

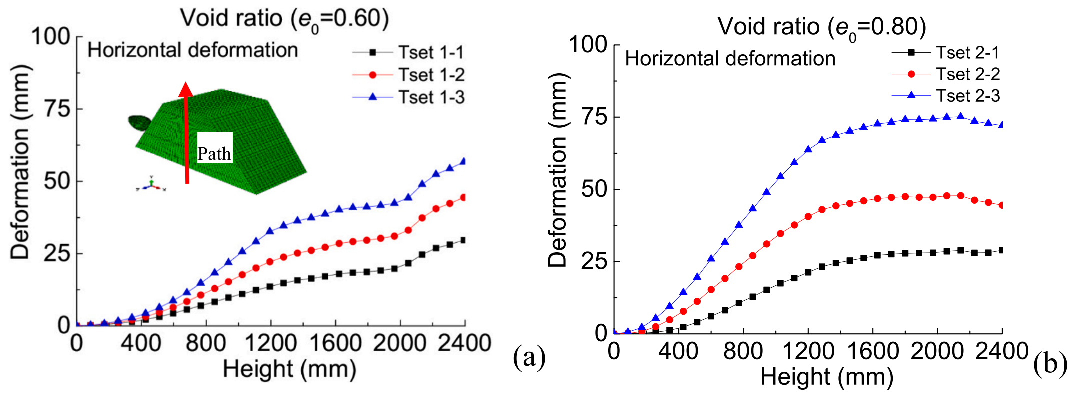

Fig. 18. Effect of repeated impacts on the Horizontal deformation of GREs with varied void ratio: (a) $e_0 = 0.6$ and (b) $e_0 = 0.8$.

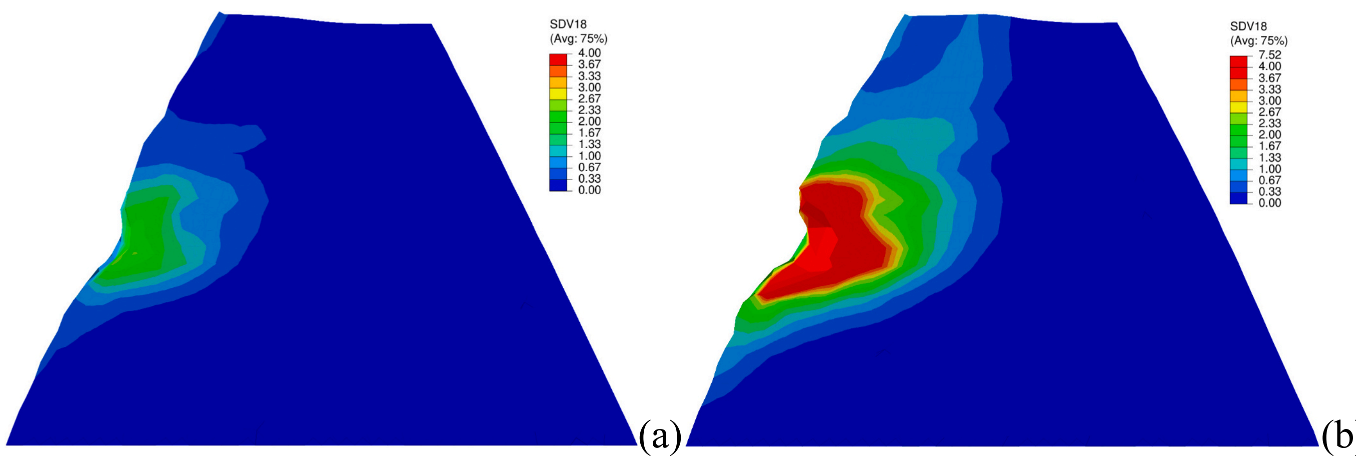

Fig. 19. Equivalent plastic strain distribution in GRE with $e_0 = 0.6$ after (a) the first impact and (b) the third impact.

effect on the toes of the GRE when sand density is larger.

3.2. Impact stress and impact force under repeated impacts

Figs. 14 and 15 show the Mises stress and pressure distribution in the middle of the GRE before and after impact, respectively. Both the Mises stress and pressure increase after each impact, and their maximum values are observed near the impact point. In dense sand, the Mises stress and pressure after impact increase with the impact numbers. This indicates that the soil elements fail due to an increase in both mean effective stress and Mises stress. However, the soil elements fail with increasing Mises stress and decreasing pressure under repeated impacts in loose sand (Figs. 14 and 15). In GREs constructed with loose sand, repeated impacts gradually create a crater at the impact point. This crater expands with each subsequent impact. The pressure in the sand is inversely proportional to the crater area. In loose sand, the crater area increases significantly after each impact, leading to lower pressure. In dense sand, the crater area shows much less change, and therefore, the pressure increases with the impact number.

Fig. 16 shows the evolution of horizontal impact force (in the x-

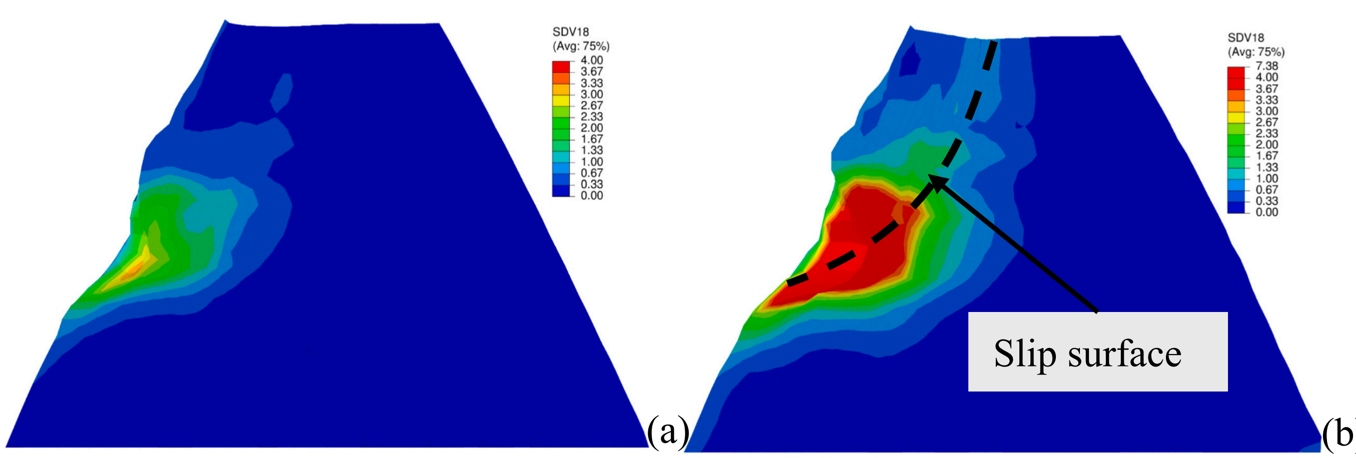

Fig. 20. Equivalent plastic strain distribution in GRE with $e_0 = 0.8$ after (a) the first impact and (b) the third impact.

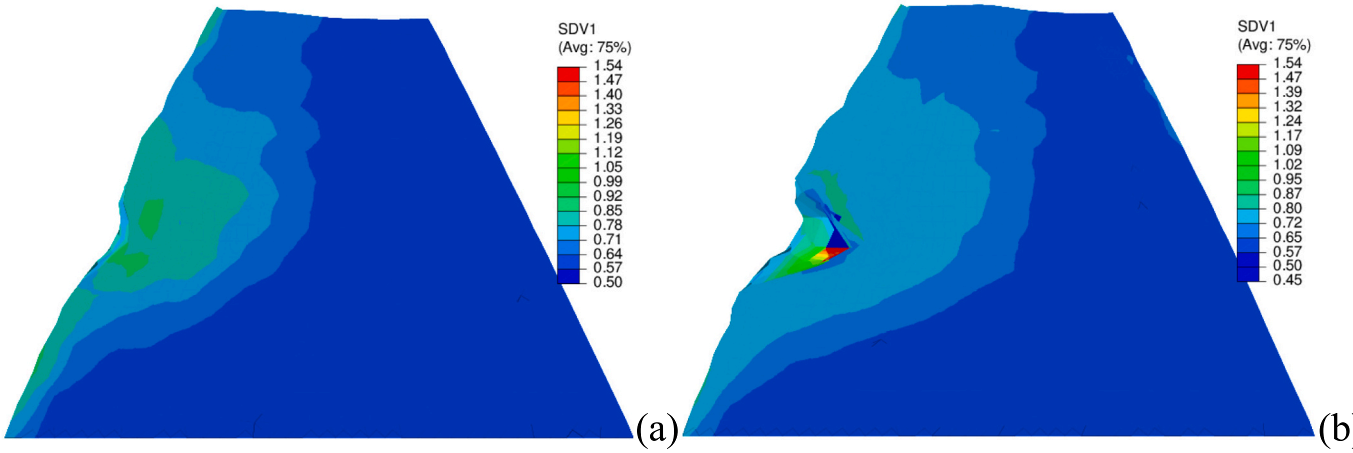

Fig. 21. Void ratio distribution in GRE with $e_0 = 0.6$ after (a) the first impact and (b) the third impact.

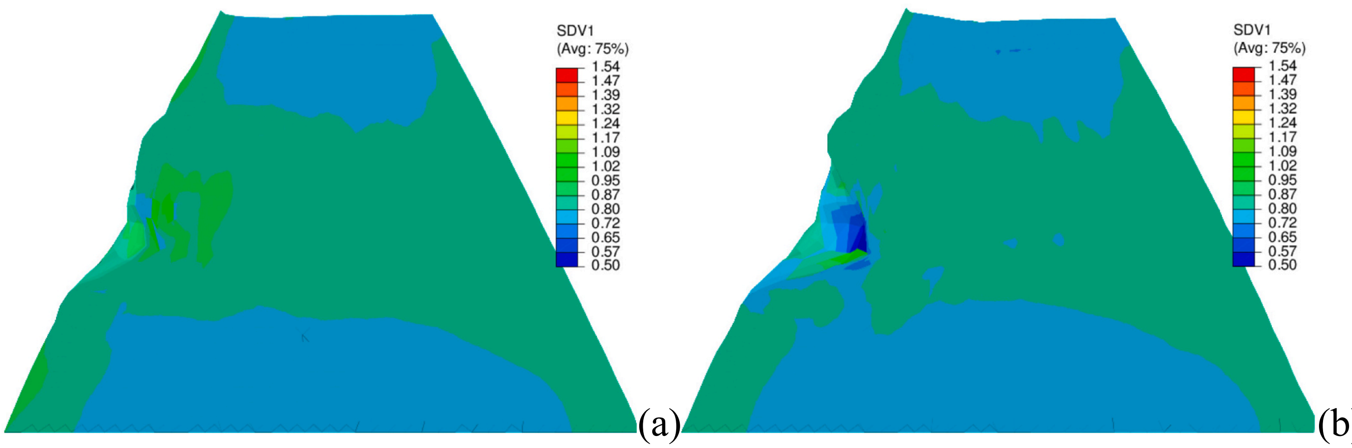

Fig. 22. Void ratio distribution in GRE with $e_0 = 0.8$ after (a) the first impact and (b) the third impact.

direction) on the GRE with different sand densities. The impact force is obtained by summing the horizontal reaction force of all nodes at the bottom of the GRE. The maximum impact force shows very little change in dense sand but increases with the number of impacts in loose sand. In the second and third impacts, the impact force before 0.03 s is negative, which is different from that in the first impact. The main reason is that the impact area of the GRE has been damaged during the first impact. In the subsequent impacts, the impact area of the GRE first tends to move towards the block, resulting in a negative impact force measured at the bottom.

3.3. Deformation and strain localisation in GREs

Fig. 17 shows the crest deformation of GREs after repeated impacts. The positive vertical displacement indicates heaving, while the negative one signifies settlement. When $e_0 = 0.6$, the closer to the mountain-side

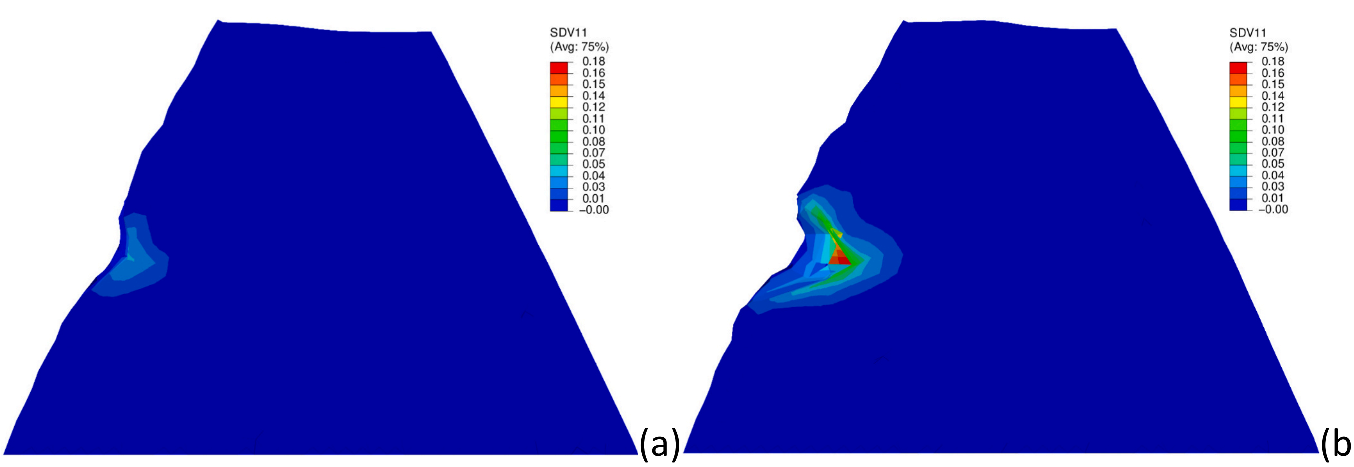

Fig. 23. Grain breakage index B_r^* distribution in GRE with $e_0 = 0.6$ after (a) the first impact and (b) the third impact.

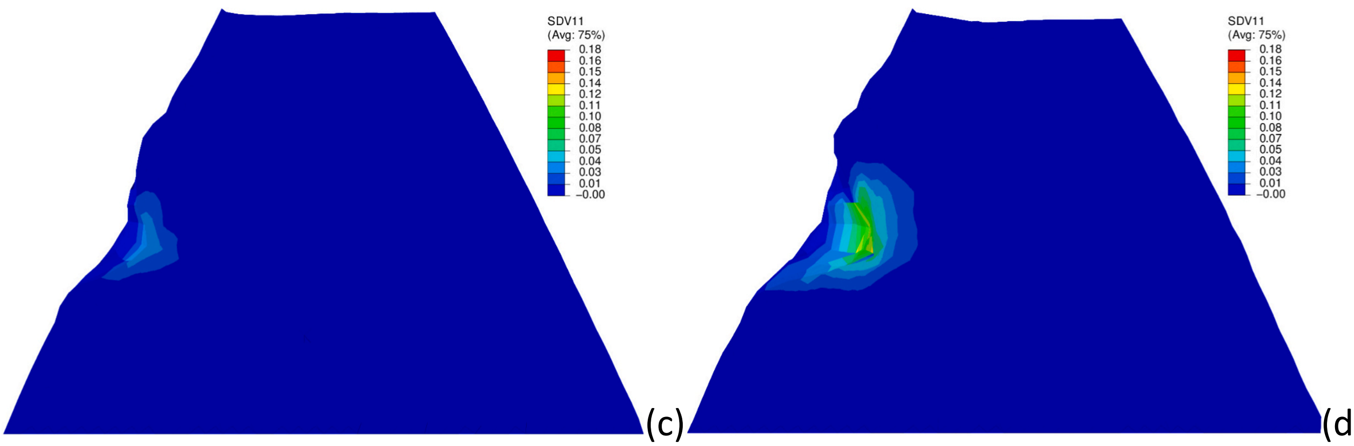

Fig. 24. Grain breakage index B_r^* distribution in GRE with $e_0 = 0.8$ after (a) the first impact and (b) the third impact.

face (impact side), the greater the heaving, which decreases with the number of impacts. Repeated impacts cause heaving accumulation in the middle part of the crest. When $e_0 = 0.8$, the crest near the mountainside shows a slight settlement after the first impact and then experiences slight heaving after the third impact. The settlement reaches the maximum at the middle of the crest and the minimum at the valley side. Repeated impacts cause an increase in the settlement (Fig. 17b).

Fig. 18 illustrates the horizontal deformation of GREs under repeated impacts for two initial void ratios ($e_0 = 0.6$ and $e_0 = 0.8$). The horizontal deformation is measured from the middle part of the GREs, from bottom to top. For $e_0 = 0.6$ (Fig. 18a), the maximum horizontal deformation is observed near the top of the GRE, with deformation increasing rapidly along the embankment height. This indicates a localised response with higher stiffness and resistance near the base. In contrast, for $e_0 = 0.8$ (Fig. 18b), the deformation is more widely distributed, extending higher along the embankment. Although loose sand exhibits greater overall deformation due to its lower stiffness and higher compressibility, it effectively distributes stresses across a broader area. Both cases demonstrate increasing deformation with repeated impacts, but the rate of increase is more pronounced in loose sand, particularly near the embankment's base. These findings suggest that GREs constructed with dense sand provide higher localised resistance.

Figs. 19 and 20 show the equivalent plastic strain (EPS) distribution in GREs with different e_0. To avoid the impact of geosynthetics on the observation of EPS changes in sand, they are not shown in these figures. As expected, the EPS is larger in the GRE with a bigger e_0. Strain localisation occurs around the impact area after the first impact. After the third impact, the strain localisation extends to the top of GREs built with both dense and loose sand. A clear shear band can be observed in loose sand after the third impact (Fig. 20). In dense sand, a shear band has just started to form at the end of the third impact, and a fully developed one is impacted after more impacts.

The void ratio distribution after impact is shown in Figs. 21 and 22. After the first impact, there is a significant increase in the void ratio (volume expansion) in the vicinity of the impact point. However, this part becomes denser after the third impact. The void ratio distribution in GRE varies with e_0. In dense sand with $e_0 = 0.6$, the top, bottom, and the area closer to the impact point of the GRE show more volume expansion. The area of volume expansion spreads towards the valley side after the third impact. Such volume expansion causes the heaving of GRE at the crest as shown in Fig. 21. In loose sand with $e_0 = 0.8$, volume expansion mainly occurs in the middle of the GRE. Volume contraction is observed at the top and bottom of the GRE (Fig. 22). Therefore, settlement is observed at the top of the GRE built with loose sand.

Figs. 23 and 24 illustrate the impact of different e_0 on the distribution of the Grain Breakage Index (B_r^*). Positive B_r^* indicates the occurrence of grain breakage, with higher values signifying a greater degree of breakage. In dense sand, the degree of breakage on the GRE surface is higher, but the range of breakage is smaller. Conversely, in loose sand, the degree of breakage is lower, but the range of breakage is wider. However, it should be emphasised that the particle breakage is not significant in these tests because high stress occurs only near the impact area.

4. Conclusions

The response of GREs built with sand wrapped by geosynthetics is investigated using finite element modelling. A DYS model that accounts for the effect of density and pressure on sand response is used. GREs with two different void ratios are simulated. A GRE built with very loose sand is modelled to investigate the effect of sand density on the GRE response. The main conclusions are:

1. The impact energy is converted to plastic dissipation in sand, friction dissipation and strain energy in both sand and geosynthetics. There is more plastic dissipation in the GRE with loose sand due to more plastic strain accumulation.
2. Under repeated impacts, the soil elements in dense sand reach failure with increasing Mises stress and mean effective stress. However, loose sand reaches failure as the mean effective stress decreases and Mises stress increases.
3. Strain localisation appears around the impact area after the first impact. A clear failure surface can be observed after the third impact in loose sand, which starts at the impact point and ends on the top of the GRE. In dense sand, a fully developed shear band is expected after more impacts.
4. There is heaving on the top of GRE with dense sand which is caused by volume expansion in the soil after impact. In the GRE with loose sand, slight heaving occurs near the mountain side and settlement dominates in the remaining par, which is due to the volume contraction of sand at the top and bottom parts of the GRE.

This study has shown that GRE built with very loose sand can also sustain multiple impacts without collapsing. There are two main reasons for this. First, loose sand can dissipate a significant amount of impact energy due to the plastic strain accumulation. Secondly, the sand has been wrapped by geosynthetics which strengthens the soil and prevents collapsing. In practical design, dense sand is still preferred as it shows less deformation accumulation after repeated impacts. However strict density control may not be very important when geosynthetics with sufficient stiffness and strength are used, which will be investigated in the future by small-scale and full-scale field tests.

CRediT authorship contribution statement

Xin Li: Writing – review & editing, Writing – original draft, Visualization, Methodology, Investigation, Conceptualization. **Zhiwei Gao:** Writing – review & editing, Writing – original draft, Methodology, Investigation, Funding acquisition, Formal analysis, Conceptualization. **Liang Lu:** Methodology, Funding acquisition, Conceptualization.

Declaration of competing interest

The authors declare the following financial interests/personal relationships which may be considered as potential competing interests:

Dr. Zhiwei Gao reports financial support was provided by The Royal Society. If there are other authors, they declare that they have no known competing financial interests or personal relationships that could have appeared to influence the work reported in this paper.

Acknowledgements

This research is funded by the Royal Society (International Exchanges Cost Shar Scheme; Grant number: IEC\NSFC\223020) and the National Natural Science Foundation of China (Grant number 52178314). The authors would like to thank Prof. Yinfu Jin at Shenzhen University for providing the VUMAT code for the sand model used in this study.

Data availability

The research data presented in the present paper is available upon request.

References

Agliardi, F., Crosta, G.B., Frattini, P., 2009. Integrating rockfall risk assessment and countermeasure design by 3D modelling techniques. Nat. Hazards Earth Syst. Sci. 9 (4), 1059–1073. https://doi.org/10.5194/nhess-9-1059-2009.

Aminata, D., Yashima, A., Sawada, K., Sung, E., 2008. New protection wall against rockfall using a ductile cast iron panel. J. Nat. Disast. Sci. 30 (1), 25–33. https://doi.org/10.2328/jnds.30.25.

Andria-Ntoanina, I., Canou, J., Dupla, J.C., 2010. Caractérisation mécanique du sable de Fontainebleau NE34 à l'appareil triaxial sous cisaillement monotone. Laboratoire Navier – Géotechnique. CERMES, ENPC/LCPC.

Bertolo, P., Oggeri, C., Peila, D., 2009. Full-scale testing of draped nets for rock fall protection. Can. Geotech. J. 46 (3), 306–317. https://doi.org/10.1139/T08-126.

Bertrand, D., Trad, R., Dorren, L.K.A., 2013. Dynamic rockfall risk analysis. Eng. Geol. 159, 152–164. https://doi.org/10.1016/j.enggeo.2013.03.010.

Bourrier, F., Lambert, S., Baroth, J., 2015. A reliability-based approach for the design of rockfall protection fences. Rock Mech. Rock. Eng. 48, 247–259. https://doi.org/10.1007/s00603-013-0540-2.

Brunet, G., Giacchetti, G., Bertolo, P., Peila, D., 2009. Protection from high energy rockfall impacts using Terramesh embankment: Design and experiences. In: Proc. 60th Highway Geology Symp., Buffalo, New York, pp. 107–124.

Celik, M., 2023. Investigating the performance of passageway corridor for ground reinforced embankments against rockfall. J. Mount. Sci. 20, 15–30. https://doi.org/10.1007/s11629-022-7559-3.

Dassault Systèmes, 2023. Abaqus User's Guide. Version 2023. Dassault Systèmes Simulia Corp, Providence, RI, USA.

Di Prisco, C., Vecchiotti, M., 2006. A rheological model for the description of boulder impacts on granular strata. Geotechnique 56 (7), 469–482. https://doi.org/10.1680/geot.2006.56.7.469.

Gao, Z.W., Zhao, J.D., Li, X.-S., Dafalias, Y.F., 2014. A critical state sand plasticity model accounting for fabric evolution. Int. J. Numer. Anal. Methods Geomech. 38 (4), 370–390. https://doi.org/10.1002/nag.2211.

Gao, Z.W., Zhao, J.D., Li, X., 2021. The deformation and failure of strip footings on anisotropic cohesionless sloping grounds. Int. J. Numer. Anal. Methods Geomech. 45 (10), 1526–1545. https://doi.org/10.1002/nag.3212.

Gao, Z., Lu, D., Hou, Y., Li, X., 2023. Constitutive modelling of fabric effect on sand liquefaction. J. Rock Mech. Geotech. Eng. 15 (4), 926–936. https://doi.org/10.1016/j.jrmge.2022.06.002.

Guzzetti, F., Reichenbach, P., Stark, C.P., Parise, M., 2005. Rockfall hazard and risk assessment along a transportation corridor in the Nera Valley, Central Italy. Environ. Manag. 35 (5), 527–538. https://doi.org/10.1007/s00267-004-0216-3.

Hungr, O., Leroueil, S., Picarelli, L., 2014. The Varnes classification of landslide types, an update. Landslides 11 (2), 167–194. https://doi.org/10.1007/s10346-013-0436-y.

Jin, Y.F., Yin, Z.Y., Wu, Z.X., Daouadji, A., 2018. Numerical modeling of pile penetration in silica sands considering the effect of grain breakage. Finite Elem. Anal. Des. 144, 15–29. https://doi.org/10.1016/j.finel.2018.02.003.

Kister, B., Fontana, O., 2011. On the evaluation of rockfall parameters and the design of protection embankments – a case study. In: Proceedings of Interdisciplinary Workshop on Rockfall Protection - Rocexs 2011, Innsbruck, Austria, pp. 31–32.

Korini, O., Bost, M., Rajot, J.-P., Bennani, Y., Freitag, N., 2021. The influence of geosynthetics design on the behavior of reinforced soil embankments subjected to rockfall impacts. Eng. Geol. 286, 106054. https://doi.org/10.1016/j.enggeo.2021.106054.

Lambert, S., Bourrier, F., 2013. Design of rockfall protection embankments: a review. Eng. Geol. 154, 77–88. https://doi.org/10.1016/j.enggeo.2012.12.012.

Lambert, S., Kister, B., 2017. Analysis of Existing Rockfall Embankments of Switzerland (AERES); Part A: State of Knowledge. Federal Office for the Environment, Bern, p. 55.

Lambert, S., Kister, B., 2018. Efficiency assessment of existing rockfall protection embankments based on an impact strength criterion. Eng. Geol. 243, 1–9. https://doi.org/10.1016/j.enggeo.2018.06.008.

Liang, J.Y., Lu, D.C., Du, X.L., Ma, C., 2020. Non-orthogonal elastoplastic constitutive model for sand with dilatancy. Comput. Geotech. 118, 103329. https://doi.org/10.1016/j.compgeo.2019.103329.

Lu, L., Liang, X., Wang, Z.J., Tang, T.T., Arai, K., 2021. Experimental testing of ground reinforced embankments under low-energy impact of rockfall. Rock Mech. Rock. Eng. 54 (11), 5667–5681. https://doi.org/10.1007/s00603-021-02573-1.

Ma, S., Lu, L., Song, A., Wang, Z., Xiao, L., Arai, K., 2024. Experimental and numerical investigation of prestressed geosynthetic-reinforced embankment subjected to traffic loading. Int. J. Geomech. 24 (1). https://doi.org/10.1061/ijgnai.gmeng-7815.

Maheshwari, S., Bhowmik, R., 2024. Performance assessment of a protection embankment designed for a rockfall-prone slope along the Lesser Himalayas of Jammu and Kashmir, India. Nat. Hazards. https://doi.org/10.1007/s11069-024-06959-6.

Maheshwari, S., Bhowmik, R., Cuomo, S., 2024. Impact performance of unreinforced and geogrid-reinforced rockfall protection embankments. Geosynth. Int. 19 (6), 1–21. https://doi.org/10.1680/jgein.23.00159.

Moon, T., Oh, J., Mun, B., 2014. Practical design of rockfall catchfence at urban area from a numerical analysis approach. Eng. Geol. 172, 41–56. https://doi.org/10.1016/j.enggeo.2014.01.004.

Moos, C., Bontognali, Z., Dorren, L., Jaboyedoff, M., Hantz, D., 2022. Estimating rockfall and block volume scenarios based on a straightforward rockfall frequency model. Eng. Geol. 309, 106828. https://doi.org/10.1016/j.enggeo.2022.106828.

Oggeri, C., Ronco, C., Vinai, R., 2021. Validation of numerical D.E.M. Modelling of geogrid reinforced embankments for rockfall protection. Geoingegneria Ambientale e Mineraria 58 (2(3)), 36–45. https://doi.org/10.19199/2021.163-164.1121-9041.036.

Peila, D., 2012. Ground reinforced embankments for rockfall protection: From real scale tests to numerical modelling. In: Lambert, S., Nicot, F. (Eds.), Rockfall Engineering. Wiley, New York, pp. 393–426. ISTE Ltd, London.

Peila, D., Ronco, C., 2009. Technical note: Design of rockfall net fences and the new ETAG 027 European guideline. Nat. Hazards Earth Syst. Sci. 9 (4), 1291–1298. https://doi.org/10.5194/nhess-9-1291-2009.

Peila, D., Oggeri, C., Castiglia, C., 2007. Ground reinforced embankments for rockfall protection: design and evaluation of full scale tests. Landslides 4, 255–265. https://doi.org/10.1007/s10346-007-0086-7.

Pérez-Rey, I., Riquelme, A., González-de Santos, L.M., Estévez-Ventosa, X., Tomás, R., Alejano, L.R., 2019. A multi-approach rockfall hazard assessment on a weathered granite natural rock slope. Landslides 16, 2005–2015. https://doi.org/10.1007/s10346-019-01255-1.

Ronco, C., Oggeri, C., Peila, D., 2009. Design of reinforced ground embankments used for rockfall protection. Nat. Hazards Earth Syst. Sci. 9, 1189–1199. https://doi.org/10.5194/nhess-9-1189-2009.

Shen, W.G., Zhao, T., Dai, F., Jiang, M.J., Zhou, G.D., 2019. DEM analyses of rock block shape effect on the response of rockfall impact against a soil buffering layer. Eng. Geol. 249, 60–70. https://doi.org/10.1016/j.enggeo.2018.12.011.

Stoffel, M., Trappmann, D.G., Coullie, M.I., Ballesteros Cánovas, J.A., Corona, C., 2024. Rockfall from an increasingly unstable mountain slope driven by climate warming. Nat. Geosci. 1-6. https://doi.org/10.1038/s41561-024-0103-5.

Tran, P.V., Maegawa, K., Fukada, S., 2013. Experiments and dynamic finite element analysis of a wire-rope rockfall protective fence. Rock Mech. Rock. Eng. 46, 1183–1198. https://doi.org/10.1007/s00603-012-0340-0.

Turner, A.K., Schuster, R.L., 2012. Rockfall characterization and control. Transp. Res. Board Nat. Acad. Sci. Washington D.C, 658. https://doi.org/10.2113/gseegeosci.19.4.398.

Uesugi, M., Kishida, H., Tsubakihara, Y., 1989. Friction between sand and steel under repeated loading. Soils Found. 29 (3), 127–137. https://doi.org/10.3208/sandf1972.29.3_127.

Volkwein, A., Gerber, W., 2011. Stronger and lighter-evolution of flexible rockfall protection systems. In: In IABSE-IASS 2011 London Symposium Report: Taller, longer, Lighter. IABSE, Zurich, Switzerland.

Wang, G.S., Li, Z.H., Liang, J.Y., Lu, D.C., Du, X.L., 2024. A state-dependent non-orthogonal elastoplastic constitutive model for sand. Comput. Geotech. 166, 105960. https://doi.org/10.1016/j.compgeo.2023.105960.

Wyllie, D.C., 2015. Rock Fall Engineering. CRC Press, Taylor & Francis Group, p. 270.

Xiao, L., Lu, L., Lin, H., Wang, Z., Arai, K., 2023. Deformation behavior and damage assessment of ground reinforced embankments impacted by multiple medium-energy rockfalls. Rock Mech. Rock. Eng. 56 (11), 8359–8374. https://doi.org/10.1007/s00603-023-03497-8.

Yan, P., Zhang, J., Kong, X., Fang, Q., 2020. Numerical simulation of rockfall trajectory with consideration of arbitrary shapes of falling rocks and terrain. Comput. Geotech. 122, 103511. https://doi.org/10.1016/j.comgeo.2020.103511.

Yao, Y.P., Sun, D.A., Luo, T., 2004. A critical state model for sands dependent on stress and density. Int. J. Numer. Anal. Methods Geomech. 28 (4), 323–337. https://doi.org/10.1002/nag.340.